Anisotropy-independent packing of confined hard ellipses

Eduardo Basurto and Gerardo Odriozola*

Área de Física de Procesos Irreversibles, División de Ciencias Básicas e Ingeniería,
Universidad Autónoma Metropolitana-Azcapotzalco,
Av. San Pablo 180, 02200 CD México, Mexico

Péter Gurin and Szabolcs Varga

Institute of Physics and Mechatronics, University of Pannonia, P.O. Box 158, Veszprém H-8201, Hungary
(Dated: 2020-12-22)

We have examined the close-packed structure and ordering properties of hard ellipses between two parallel hard walls by using geometrical conjectures and Monte Carlo simulations. Starting from closely packed hard disk structures, we discover two competing densest packings of ellipses with the stretching of hard disks into different directions. We find that parallel and tilted close-packed structures alternate with widening pore width up to the two-dimensional bulk limit, where both structures produce the same close packing value ($\eta = \pi/\sqrt{12}$). Our results highlight that the densest packing does not depend on the aspect ratio of the ellipse. This universal behavior is confirmed for three different aspect ratios ($\kappa =$ 2, 3, and 4) using replica exchange Monte Carlo simulation. Our simulation results show that even the global phase diagram is universal, where layering transitions between parallel structures and tilted-parallel structural changes are present.

I. INTRODUCTION

Systems of hard particles are known to show rich phase diagrams [1–8], despite the fact that their components lack any attractive interaction. Indeed, this kind of system is usually referred to as athermal, since temperature plays no role in their equilibrium structure. In such systems, particle shape, the presence of confinement, and the geometry of the confining walls importantly affect the phase behavior [3, 5, 9–20]. They most frequently occur at nano and mesoscale levels but can also appear in the macroscopic world. In the first case, temperature fluctuations drive the systems to equilibrium. In the second one, one must externally inject energy in the way of tapping movements [21–23] or container twists [24] to make the system travel through configurational space.

By quasi-statically increasing the pressure of this kind of system while keeping equilibrium, it is possible to approach the maximal packing fraction [25]. Thus, at infinite pressure, the thermodynamics of hard particles converge to a geometrical problem, i. e. the packing of particles. As early as 1611, Kepler proposed his famous conjecture stating that, in the three-dimensional Euclidean space, the maximal attainable packing fraction of spheres corresponds to a degenerate family of structures where the face-centered cubic and the hexagonal close packing arrangements are among them. These structures yield the packing fraction $\pi/\sqrt{18}$. Thus, it can be safely said that packing is an ancient problem. In addition, packing plays a crucial role in several practical applications spanning different time-space scales. These include atomistic scales, such as the study of solids [26], liquids [27], and glasses [28], and macroscopic scales, such as the design of satellite modules and space stations [29], passing through intermediate scales, such as the macromolecule domain [30], the colloidal domain [31, 32], and the micron-size domain [33].

Ellipses are two-dimensional geometrical shapes, very relevant in astronomy and physics. They describe the trajectories of celestial bodies and are the most simple shapes when composing two harmonic movements with the same frequency in orthonormal directions. This last fact is related to elliptically polarized light. They are usually seen as the generalization of the circle since they can be mathematically expressed in a very similar way, and the circle shape is regained by setting equal the lengths of their main axes. The intersection of a cone or a cylinder with a tilted plane produces an ellipse. Also, the curve encloses a couple of focal points in such a way that the sum of the two distances from them to any point of the ellipse is constant. Systems composed of hard ellipses were studied in both bulk [1, 6, 34] and confinement [19, 35–37].

This work deals with these three concepts, namely, phase diagrams of hard particles, packing, and ellipses. We propose some candidate structures to yield the maximal packing fraction of ellipses confined by parallel walls, as explained in the following section. The obtained maximal packing fraction does not depend on the ellipse's anisotropy. To confirm that the conjectured structures produ´ce the maximal packing fraction, we perform replica-exchange Monte Carlo (REMC) simulations of confined hard ellipses with several aspect ratios and confining distances. In this regard, section II is devoted to the maximal packing fraction, while section III presents the details of the simulations. In section IV, we present the outcomes from these simulations, which not only confirm our proposed configurations as those yielding the maximal packing fraction but also allows us to build the phase diagram of confined ellipses. The phase diagram turns out to be independent of the particle's shape anisotropy.
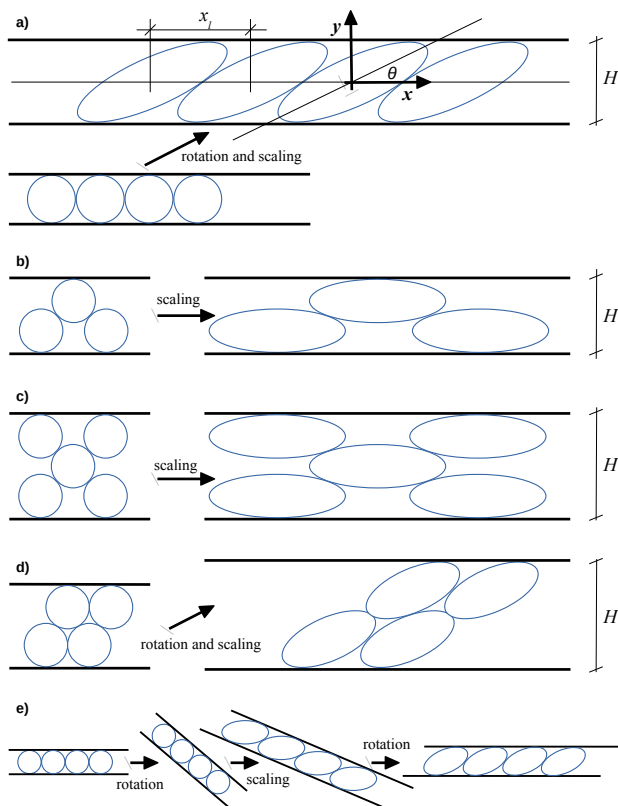
---

* godriozo@azc.uam.mx

FIG. 1. Schematic representation of the transformations applied to different circle configurations. The transformation applied in panels a) and d) involve rotations and scalings, as shown in detail in panel e). In these cases, the transformation matrix corresponds to $T(\kappa, \theta) = O(\theta^*)^{-1} S(\kappa) O(\theta)$, where O^{-1} and O are clockwise and counterclockwise rotation matrixes, respectively, S is the stretching matrix along the x direction, and $\theta^* = \tan^{-1}(\kappa \tan \theta)$.

The last section presents some concluding remarks.

II. MAXIMAL PACKING FRACTION

In this section, we explore candidate configurations for the maximal packing fraction of monodisperse ellipses confined by parallel planes. We restrict the possible configurations to those having all ellipses with the same orientation. The equation describing the perimeter of an ellipse with their main axes placed along the x and y axes is given by

$$\frac{x^2}{\sigma_b^2} + \frac{y^2}{\sigma_s^2} = \frac{1}{4}, \quad (1)$$

where σ_b and σ_s are the lengths of the big and small diameters, i.e. the major and minor lengths of the ellipse, respectively. By introducing the aspect ratio as $\kappa = \sigma_b/\sigma_s$, forcing $\sigma_s = 1$, and rotating the ellipse an angle θ counterclockwise around the axis perpendicular to the

xy-plane passing through its center (see Fig. 1 a)), the equation takes the form

$$\frac{(x\cos(\theta) - y\sin(\theta))^2}{\kappa^2} + (x\sin(\theta) + y\cos(\theta))^2 = \frac{1}{4}. \quad (2)$$

By forcing the derivative of function $y(x)$ to zero, one can get that the maximum value of y is given by

$$y_m = \frac{\sqrt{\kappa^2 - (\kappa^2 - 1)\cos^2(\theta)}}{2}, \quad (3)$$

at

$$x_m = \frac{(\kappa^2 - 1)\sin(2\theta)}{8y_m}. \quad (4)$$

Besides, the length of the line segment of the x-axis intersecting the ellipse, x_l, can be obtained by setting $y(x) = 0$. This leads to

$$x_l = \frac{\kappa}{4y_m}. \quad (5)$$

Thus, the packing fraction of a close-packed single layer of parallel ellipses, all touching the two confining walls, is

$$\eta = \frac{\pi \sigma_b \sigma_s}{4H 2x_l} = \frac{\pi \kappa}{8H x_l} = \frac{\pi}{4}, \quad (6)$$

where $H = 2y_m \leq \kappa$ is the distance between the confining planes, see Fig. 1 a). Note that the result given by Eq. (6) is independent of the angle θ and the aspect ratio, κ, and so it is identical to the one corresponding to the packing of a single layer of disks for $H = 1$. Indeed, a combination of rotation and scaling in a single direction is a type of affine transformation that preserves η [38] (see panel a) of Fig. 1). Due to this reason, hard ellipses fill the 2d space with the same packing fraction as that of disks, contrasting with the 3d case where ellipsoids can arrange in layers having different directions [39–42]. The domain of Eq. (6) has the lower limit $H = \sigma_s = 1$ and the higher limit $H = \sigma_b = \kappa$. These limits correspond to the stretching of the layer of disks along the parallel and perpendicular to the direction of the confining walls, respectively.

Up to this point, it is clear that the maximal packing fraction cannot be less than $\eta = \pi/4$. Nonetheless, we can test other arrangements to explore higher possible η values. We can, for instance, horizontally scale the packing configuration given at the left of Fig. 1 b). As mentioned, by doing so, the packing fraction is preserved, allowing for an easy determination of η. It reads

$$\eta^p(H) = \frac{\pi(\sigma_s/2)^2}{H\sqrt{\sigma_s^2 - (H - \sigma_s)^2}} = \frac{\pi}{4H\sqrt{2H - H^2}}, \quad (7)$$

for $1 \leq H \leq 1 + \sqrt{3}/2$ (recall that $\sigma_s = 1$). Here, superscript p stands for parallel, since this horizontal scaling produces ellipses with their main axes parallel to the walls. Note that the condition $H = 1$ gives the
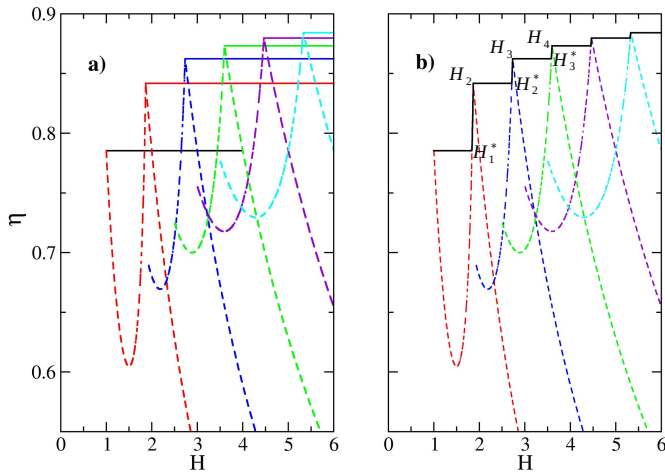
FIG. 2. a) Packing fraction, η, as a function of the distance between plates, H, for $\kappa = 4$. The dashed lines correspond to $\eta^p(H,n)$ given by Eq. (8), whereas the solid lines correspond to $\eta^t(H,n)$ given by Eq. (9). Lines corresponding to single, double, triple, cuadruple, quintuple, and sextuple layers are colored black, red, blue, green, violet, and cyan, respectively. Panel b) replicates panel a) but it also includes the maximal packing fraction, $\eta^m(H) = \max[\eta^t(H,n),\eta^p(H,n+1)]$, as a black thick solid line. This panel holds for $\kappa \gtrsim 1.8393$.

single-layer arrangement with $\eta = \pi/4$. The other limit, $H = 1 + \sqrt{3}/2$, corresponds to the packing of two compact layers of circles, see Fig. 1 d) left, and to a maximum of $\eta^p(H)$. For $H > 1 + \sqrt{3}/2$ the planes cannot touch both layers of particles, and the packing fraction yields $\eta^p(H) = \pi/(2H)$. Note that $\eta^p(H)$ does not depend on κ.

Fig. 1 c) shows the scaling of a three-layer arrangement of disks, which can also be done for n layers. For $n \geq 2$, this leads to a general expression for $\eta^p(H,n)$ and this type of arrangement. It reads

$$\eta^p(H,n) = \begin{cases} \dfrac{n\pi}{8H\sqrt{1-\left(\frac{H-1}{n-1}\right)^2}} & \text{for } \frac{n+1-\delta_{n,2}}{2} \leq H \leq H_n \\ \dfrac{n\pi}{4H} & \text{for } H > H_n, \end{cases} \quad (8)$$

where $H_n = 1 + \sqrt{3}(n-1)/2$. For $H > H_n$ the configuration is not compact. Note that Eq. (8) reproduces Eq. (7) for $n = 2$. The same happens with the upper limit $1 + \sqrt{3}(n-1)/2$ and the packing fraction $\eta^p(H,n) = n\pi/(4H)$. Again, Eq. (8) does not depend on κ.

Finally, it is also possible to scale the most dense-packed arrangement for a given number of layers, n, in a non-horizontal direction, as shown in Fig. 1 d). This allows us to increase H from $1 + \sqrt{3}(n-1)/2$ to $(1 + \sqrt{3}(n-1)/2)\kappa$ with a fixed η value by varying the scaling direction from horizontal to vertical, leading to

$$\eta^t(H,n) = \frac{n\pi}{2(2+\sqrt{3}(n-1))}, \quad (9)$$

where the superscript t stands for tilted. Note that this expression for $\eta^t(H,n)$ is a monotonically increasing function of n. In fact, for n and $H \to \infty$ this quantity goes to $\pi/\sqrt{12}$, the maximum packing fraction of circles and ellipses in a 2d Euclidean space. We speculate this is the highest possible packing fraction for most of the H domain, except for tiny regions where Eq. (8) yields larger values. By taking these two possibilities into account, the maximal packing fraction, $\eta^m(H)$, is simply defined as the maximum value from Eqs. (8) and (9), i. e. $\eta^m(H) = \max[\eta^t(H,n),\eta^p(H,n+1)]$.

The H_n^* value at which the n-layer tilted structure with a packing fraction given by $\eta^t(H,n)$ is superseded with the $(n+1)$-layer parallel structure corresponding to $\eta^p(H,n+1)$ is given by (see Fig. 2)

$$H_n^* = \frac{1}{2} + v + \frac{1}{2}\sqrt{\frac{2}{3} + n^2\left(\frac{4}{3} + v^{-1}\right) + w} \quad (10)$$

where

$$v = \frac{\sqrt{1 + 2n^2 - 3w}}{2\sqrt{3}},$$

$$w = \frac{y}{3 \cdot 2^{1/3} z^{1/3}} - \frac{z^{1/3}}{3 \cdot 2^{1/3}},$$

$$z = x + \sqrt{x^2 + y^3},$$

$$y = -2^{2/3}\left(n^4 - 2n^2 + 12a + 1\right),$$

$$x = 108a - 72a\left(1 - n^2\right) + 2\left(1 - n^2\right)^3,$$

and

$$a = \left[\frac{(n+1)}{4}\left(2 + \sqrt{3}(n-1)\right)\right]^2.$$

Expression (10) corresponds to the largest of the two real roots resulting from a fourth-order polynomial in H coming from the equation $\eta^t(H,n) = \eta^p(H,n+1)$. Note that $y^3 + x^2 < 0$ when $n > 17$, and so z turns into a complex number. Nonetheless, w and H keep being real. It can be proved that in the limit of large n Eq. (10) asymptotically goes to

$$H_{n+1} = \frac{\sqrt{3}}{2}n + 1, \quad (11)$$

the point at which Eq. (8) reaches its maximum value for the $(n+1)$-layer (see Fig. 2). This means that the range at which $\eta^p(H,n+1)$ is maximum, $H_n^* < H \leq H_{n+1}$, goes to zero with increasing n.

The Eqs. (8) and (9) defining $\eta^p(H,n)$ and $\eta^t(H,n)$, respectively, are employed to build Fig. 2 for $\kappa = 4$ and $H < 6.0$. In Fig. 2 a), the black solid line corresponds to the packing fraction of a single layer of packed ellipses, $\pi/4$. As mentioned, the domain of this line is $1 \leq H \leq 4$. Cases with $n = 2$, 3, 4, 5, and 6, are shown with red, blue, green, violet, and cyan colors, respectively. Also, we use dashed lines to represent data as obtained from Eq. (8) and solid

ones for Eq. (9). The packing improves by increasing H in such a way that the maximal packing fraction looks like a monotonously increasing step function. These steps are not discontinuous but follow Eq. (8) in $H_n^* < H \leq H_{n+1}$. Only in these H domains, Eq. (8) produces larger values than those given by the horizontal lines, Eq. (9). The behavior of the maximal packing fraction is highlighted in Fig. 2 b). There it turns clear how the H regions where $\eta^p(H, n+1)$ yields the maximal packing fraction shrink with increasing n. Also, augmenting n makes the height of the $\eta^p(H, n)$ steps smaller.

Since Eqs. (8) and (9) are κ-independent, Fig. 2 a) exhibits an unusual κ independence except for the H domains of the horizontal lines. This has no impact on Fig. 2 b) for all $\kappa \geq H_1^* \approx 1.8393$. For smaller κ, one should be aware that the tilted and compact single-layer cannot hold up to $H = H_1^*$, which would lead to a decrease of η before the parallel two-layer arrangement takes the leading packing fraction. In this work, we are restricting to cases with $\kappa \geq 2$, where $\eta^m(H)$ is irrespective of κ.

III. SIMULATION DETAILS

We have performed REMC simulations that are particularly useful to sample from uneven free energy landscapes [43, 44] and are usual at high packing fractions. For this purpose, the partition function of an extended ensemble Q_{ext} is defined as the product of the partition functions of N_r ensembles, $Q_{\text{ext}} = \prod_i^{N_r} Q_i$, where Q_i is the ensemble i. As done in previous works [25, 45–47], to deal with systems of hard particles we employ an expansion of the isobaric ensemble [48], i.e. $Q_i = Q(N, P_{x,i}, T)$. Here, N, T, and $P_{x,i}$ are the number of particles, the temperature, and the component applied along the channel of the two-dimensional pressure tensor of the ensemble i, respectively. That is, all N_r ensembles share the same N and T, but each one has a different parallel pressure component. We define N_r simulation cells each one placed in a different ensemble. Thus, each NP_xT ensemble is sampled following a standard MC procedure by each simulation cell, but there are also swap trials between the simulation boxes of ensembles with similar P_x values.

We have approached the ellipse-ellipse distance of closest approach as done in previous studies [6, 45, 49]. This distance, defined for 3D spheroids, is in turn employed to detect overlaps. It reads [50]

$$\sigma = \frac{\sigma_s}{\sqrt{1 - \frac{1}{2}\xi\left[A^+ + A^-\right] + (1-\xi)\xi'\left[A^+A^-\right]^\gamma}}, \quad (12)$$

with

$$A^\pm = \frac{(\hat{\mathbf{r}} \cdot \hat{\mathbf{u}}_i \pm \hat{\mathbf{r}} \cdot \hat{\mathbf{u}}_j)^2}{1 \pm \xi\hat{\mathbf{u}}_i \cdot \hat{\mathbf{u}}_j}, \quad (13)$$

$$\xi = \frac{\sigma_b^2 - \sigma_s^2}{\sigma_b^2 + \sigma_s^2} \quad , \quad \xi' = \left(\frac{\sigma_b - \sigma_s}{\sigma_b + \sigma_s}\right)^2. \quad (14)$$

As defined in the previous section, σ_b and σ_s are the lengths of the major and minor axes of the spheroids, respectively. Recall that we have forced $\sigma_s = 1$, so it can be used as the unit of length, and we vary σ_b to obtain different anisotropies, $\kappa = \sigma_b/\sigma_s$, such that $\kappa \geq 1$. Unit vectors $\hat{\mathbf{u}}_i$ and $\hat{\mathbf{u}}_j$ point along the smallest diameters of spheroids i and j, respectively. The unit vector $\hat{\mathbf{r}}$ points along the line that joins the geometric centers of particles i and j. The parameter γ was introduced elsewhere [49] to further approach the exact Perram and Wertheim numerical solution [51, 52]. Its values are given in reference [49]. The average difference between the analytical approach and the exact numerical solution is always small [49]. To convert this general 3D expression to the 2D case, we simply restrict the position of all spheroids and unit vectors $\hat{\mathbf{u}}$ to the xy-plane.

To introduce confinement by two walls parallel to the x-axis we make use of the maximum value of the ellipse contour projected in the y-axis, y_m. Its value is given by Eq. (3). When the difference between the y plane position ($y = \pm H/2$) and the projection of the ellipse center on y is lower than y_m, the particle and the wall overlaps. Then, we only applied periodic boundary conditions to the x direction. This way, the y-axis is bounded by the walls.

As usual, Verlet lists are employed to gain efficiency. For ellipsoids, they are defined as described elsewhere [34, 53]. We set $N_r = 128$ ensembles (and replicas) with $N = 100$. The code is implemented in Graphics Processing Units (GPUs) in such a way that each replica is handled by a single-core as described in detail elsewhere [25, 47]. Since the number of cores of our GPUs is above 2000, we are running several cases with different pore widths, H, in a single device. The swap stage is performed by the host once the necessary information is gathered by the CPU. The swaps are tried among replicas having similar pressures, $\beta P_{x,i}$ and $\beta P_{x,j}$ with $j = i + 1$ and $\beta = (k_B T)^{-1}$, with acceptance probability $\min\{1, \exp\left[(\beta P_{x,i} - \beta P_{x,j})(A_i - A_j)\right]\}$, where A_i and A_j are the areas of replicas i and j (in units of σ_s^2), respectively. To yield a similar acceptance probability for all pair of neighboring ensembles [54], we impose a geometric progression with the replica index for the values of $\beta P_{x,i}$, expanding from $\beta P_{x\min} = 0.2$ to a maximum pressure of $\beta P_{x\max} = 100$ (in units of σ_s^{-2}, recall that we have set $\sigma_s = 1$).

We start the simulations from loose random configurations or our assumed close-packed configurations, and run them until the system of replicas reaches a steady-state. Once this condition is achieved, we perform several averages that include the packing fraction, $\langle \eta \rangle = N\pi\sigma_s^2\kappa\langle A^{-1}\rangle/4$, and the dimensionless isothermal compressibility, $\chi = (4/(\pi\sigma_s^2\kappa))d\eta/d(\beta P) = N(\langle\eta^2\rangle - \langle\eta\rangle^2)/\langle\eta\rangle^2$, to determine the corresponding phase-like boundaries.
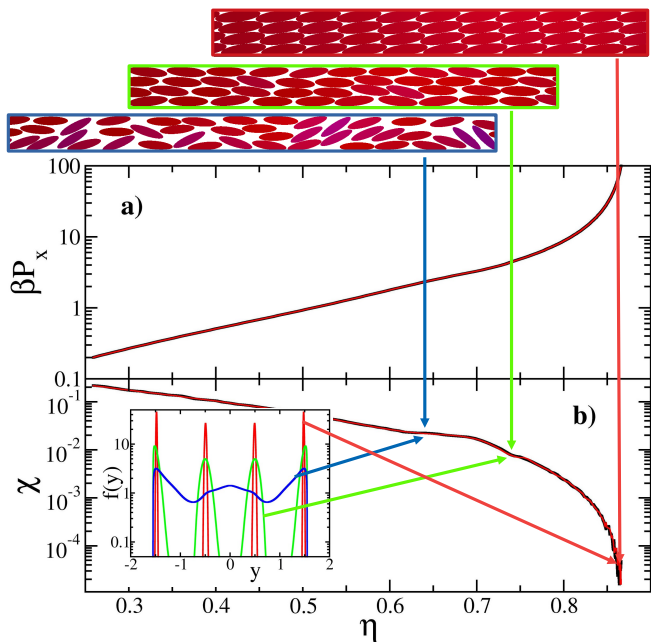
FIG. 3. a) Equation of state, given as βP_x, and b) dimensionless isothermal compressibility, χ, as a function of the area fraction, η, for $\kappa = 4$ and $H = 4.1$. The thin red and the thick black curves, which practically coincide with each other, correspond to simulations started from loose random configurations and the conjectured close-packed structure. The inset in b) shows the normalized density profiles for the cases signaled by the arrows. The snapshots at the top of the figure correspond to the same cases shown by the inset and show a partial view of the simulation cells. Colors of the arrows and frames match the colors of the curves in the inset. Parallel and perpendicular to the walls ellipses are colored red and blue, respectively. Intermediate tones are employed for midway orientations.

IV. SIMULATION RESULTS

A typical equation of state as obtained from REMC is shown in Fig. 3 a). Panel b) of the same figure shows the dimensionless isothermal compressibility, χ. Both panels show the outcomes of compression and decompression runs by starting from random configurations and the conjectured close-packed structures, respectively. These curves perfectly agree with each other, i.e. under these conditions the system of replicas is ergodic. We have included three system snapshots taken from the ensembles with the βP_x and χ values signaled by the corresponding arrows. In addition, these snapshots correspond to the density profiles given in the insert. For the sake of clarity, the colors of the snapshot frames, arrows, and density profiles match each other. With increasing pressure, we observe a fluid three-layer arrangement (blue-frame snapshot), which evolves to produce a four-layer parallel-to-the-walls configuration (green-frame snapshot), which ends into the tilted structure shown in Fig.1 d) (red-frame snapshot), whose packing fraction is given by Eq. 9 with $H = 4.1$ and $\kappa = 4$. The number of layers is captured by
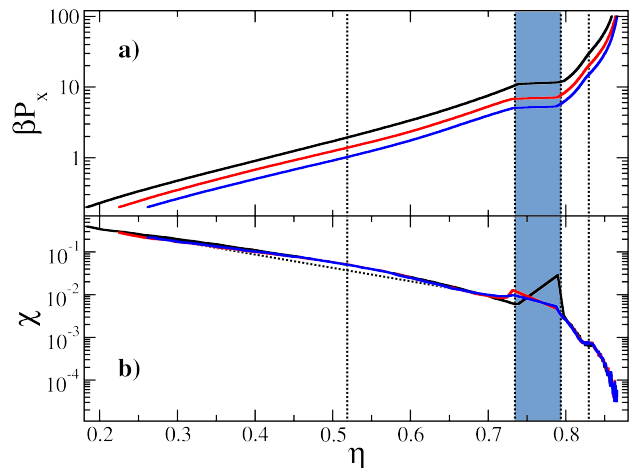

FIG. 4. a) Equation of state, given as βP_x, and b) dimensionless isothermal compressibility, χ, as a function of the occupied area fraction, η, for $H = 3.75$. Black, red, and blue lines correspond to $\kappa = 2$, 3, and 4. Vertical dotted lines signal structural transitions. The filled gap between middle dotted lines highlights a first-order-like layering transition. Data correspond to simulations started from the conjectured close-packed structure.

the normalized density profile, $f(y) = \eta(y)/\eta$, where y is the distance perpendicular to the walls measured from the center of the pore.

The monotonically increasing equation of state, $\beta P_x(\eta)$, slowly grows at low η values and diverges when approaching $\eta^t(4.1, 4) \approx 0.873$. However, its derivative (or its inverse, χ) is not a monotonic function of η. The overall behavior of χ is decreasing, but it shows some relative maxima. These maxima signal structural rearrangements shown by the snapshots of Fig. 3. Note that for this particular H value, the $n + 1$-layer parallel configuration (green-framed snapshot of Fig. 3) occurs in a relatively small η domain. This occurs despite the fact that the tilted configurations shrinks the orientational and positional configutation domains.

Given that $\eta^m(H)$ is κ-independent, questioning up to which point this independence translates to the phase diagram and the equations of states naturally arises. To answer the second part of this question we have compared several $\beta P_x(\eta)$ curves as obtained for different κ values. A typical example of this comparison is depicted in Fig. 4, for $H = 3.75$. There it is observed how the three $\beta P_x(\eta)$ curves are different, despite diverging at the same $\eta^m(H)$ value. The pressure needed to compress the system to yield a particular η value decreases with increasing κ. Nonetheless, the shapes of the $\beta P_x(\eta)$ curves are very similar. All of them show marked plateaus in the region $0.73 \lesssim \eta \lesssim 0.79$, and a soft undulation around $\eta \approx 0.83$. Indeed, their derivatives are very close to each other for all η, as signaled by the corresponding $\chi(\eta)$ curves. These functions show relative maximums at the $\beta P_x(\eta)$ plateaus and at the $\beta P_x(\eta)$ undulations, which practically occur

at the same η. Thus, even though there is no collapse of the $\beta P_x(\eta)$ curves to yield a muster one, the structural changes are practically independent of κ.

When comparing Figs. 3 and 4, we can observe that decreasing H leads to a shift of the compressibility peaks to the right, which highlights the sharpening of the corresponding transitions. Note that the peak appearing at larger densities corresponds to the change from a tilted n-layer to a parallel n-layer structure, and the second and larger one to the change from an n-layer to an $(n-1)$-layer configuration ($n = 4$ in this case). Additionally, the density of the first transition approaches $\eta^p(H, n)$ as H goes to H_n (the vertex of the $\eta^m(H)$ function after the step-like increase), which is the expected behavior since the closed packed structure turns parallel from the tilted structure at $H = H_n$. Furthermore, the density of the n-layer to an $(n-1)$-layer turns into a gap when reducing H. This gap also shifts to larger densities and disappears at $H = H^*_{n-1}$, which is also expected since below H^*_{n-1} the parallel n-structure is replaced with the tilted $(n-1)$-structure at infinite pressure.

The tilted-parallel structural change is weak because it is accompanied only by an orientational rearrangement, while the number of layers is not affected. In the case of the layering structural change, the formation of a new layer is very expensive as the translation freedom of the particles has to be strongly reduced. At $H = H^*_{n-1}$, this would correspond to a formation of an $f(y)$ with n Dirac-delta peaks. This shows that H^*_{n-1} points are singular, which renders the structural change to be critical.

Fig. 4 also shows a very wide and smooth hump of $\chi(\eta)$ (not a maximum) at around $\eta = 0.52$, as pointed out by the straight dashed line inserted in panel b). This hump is linked to a gradual change from the $(n-1)$-layer towards a more disordered structure that resembles an isotropic fluid. However, the structure is not completely isotropic, given that the presence of the confining walls always produces local orientation [36]. The hump also behaves like the other two transitions. That is, it strengthens and shifts towards larger densities by decreasing H. Indeed, it turns into the $(n-1)$-layer–$(n-2)$-layer structural transition at sufficiently low H values. In turn, the n-layer–$(n-1)$-layer strong transition occurring at larger densities smooths and shifts towards lower densities by increasing H. Eventually, the hump of $\chi(\eta)$ completely disappears at large enough H values.

The shifts of the $\chi(\eta)$ peaks with H define the phase-like boundaries of the diagram shown in Fig. 5. In this chart, we include data from $\kappa = 2$, 3, and 4. As can be seen, the data corresponding to different κ values tend to group to define a single emerging picture. In general, the number of layers, n, increases with increasing H, and the sequence $(n-1)$-parallel, n-parallel, n-tilted repeats for each step of $\eta^m(H)$. In addition, close and at the right of the lower-density vertice of each $\eta^m(H)$ step, $[H^*_{n-1}, \eta^m(H^*_{n-1})]$, there appears a coexistence-like behavior, indistinguishable from a genuine first-order transition. By approaching H^*_{n-1} with $H > H^*_{n-1}$ we get differ-
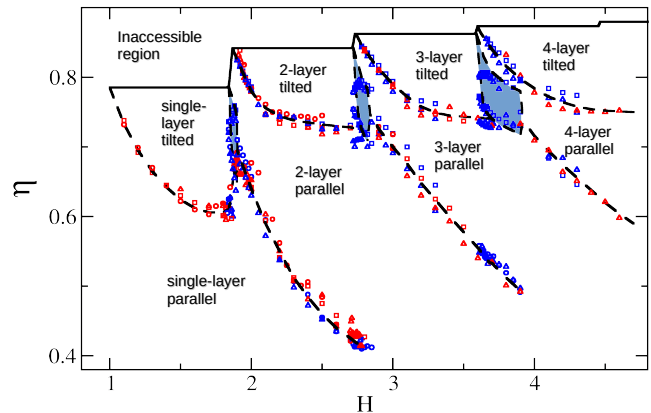

FIG. 5. Map of observed phased. The black solid line separates the accessible from the inaccessible region. Red and blue symbols correspond to the phase-like boundaries as obtained from compressing and decompressing runs, respectively. Circles, squares, and triangles correspond to $\kappa = 2$, 3 and 4. The dashed black lines are guides to the eye. The colored regions signal the coexistence of phases.

ent βP_x curves for loose random and close-packed initial conditions, pointing out the non-ergodic nature of the system. Very close to H^*_{n-1}, the REMC is unable to produce the parallel n-layer from random configurations, whereas pressure must be considerably dropped to yield the $(n-1)$-layer from the parallel n-layer configuration. In these cases, neither the obtained curves correspond to equilibrium, nor the hysteresis cycle around the coexistence can be broken. Fig. 5 only shows decompression data close to H^*_{n-1}. We plotted the expected behavior of the coexistence regions as guides to the eye. These lines depart from the data around H^*_{n-1}. However, this behavior is not observed for the parallel to tilted rearrangement when approaching the upper vertice of the $\eta^m(H)$ step.

With increasing H, the n-layer parallel arrangement smoothly gains orientational and positional freedom, allowing the particles to keep an average parallel direction while increasing the size of their orientational and positional fluctuations. Conversely, the tilted n-layer increases its tilted angle, which conserves a high packing fraction and avoids increasing orientational fluctuations. As noted, the pattern repeats for different values of n. However, it seems that the size of the coexistence region increases with n, which makes it impossible to produce a correspondence of states for different values of n, as done elsewhere [46]. We guess that the size of the coexistence should increase and reach a plateau for a sufficiently large value of n. At that point, one may attempt to yield a unified and approximate phase diagram independent of n.

The behavior of our system resembles the one found for quasi-one-dimensional confined hard squares. This system shows a strong structural transition from a tilted to a parallel to the walls arrangement of squares [46]. Here, $\beta P(\eta)$ shows a large plateau, practically a true

η discontinuity. As for confined ellipses, the transition strengthens with decreasing H, turning critical when H approaches a value at which $\eta^m(H)$ shows a kink. For squares P_x diverges at this point, with critical exponents belonging to the universality class of the one-dimensional Ising model [16, 17]. Given the similarities, we believe the same happens for the confined ellipse system at the set of points $[H_n^*, \eta^m(H_n^*)]$.

V. CONCLUSIONS

Given that the arrangement of ellipses in the 2d-Euclidean space yielding the maximal packing density is produced by scaling the triangular lattice of disks in any direction, we speculate that a similar scaling should lead to the maximal packing of ellipses confined by parallel walls. We have observed that the scaling in the parallel to the walls direction and a tilted scaling competes and alternates to yield the optimal structure with increasing H, the confining distance. The optimal packing density, $\eta^m(H)$, resembles an ever-increasing staircase function, where the heights of the steps monotonously decrease with H. However, unlike a true staircase function, the steps are not discontinuous but follow the function $\eta^p(H)$, the maximal packing for the parallel to the walls scaling. Hence, the parallel close-packing occurs only in small H ranges, and the tilted close-packed configuration rules over a large H domain. In addition, $\eta^m(H)$ asymptotically approaches the optimal packing fraction of unconfined ellipses in the 2d-Euclidean space, i.e. $\eta^m(H \to \infty) = \pi/\sqrt{12}$. It should be stressed that the obtained $\eta^m(H)$ is κ independent for $\kappa \gtrsim 1.8393$.

We have performed REMC simulations with a threefold aim: a) to observe whether simulations support or not the conjectured optimal close-packed configurations; b) to determine whether or not the κ-independence of $\eta^m(H)$ holds for the complete phase-diagram; c) to provide the full phase diagram of confined ellipses for $\kappa \gtrsim 1.8393$. We found that simulations support the conjectured optimal close-packed arrangement in all studied cases. The independence of the phase-diagram with κ was also reasonably confirmed, although the equation of states depends on κ. In general, three different arrangements appear. An $(n-1)$-layer parallel arrangement, an n-layer parallel arrangement, and an n-layer tilted configuration, with increasing pressure. In particular, the transit involving the change in the number of layers strengthens when H approaches H_{n-1}^* from above. This points to a first-order-like layering transition as H goes to H_{n-1}^*, where the formation of an additional layer is extremely hard due to the lack of translational freedom in the normal direction to the walls. This happens even though van Hove's theorem [55, 56] rules out the existence of genuine thermodynamic transitions. Nonetheless, given the similarity found between the outcomes for confined ellipses and squares [16, 17, 46], we believe $[H_n^*, \eta^m(H_n^*)]$ to be critical points.

ACKNOWLEDGMENTS

[1] J. A. Cuesta and D. Frenkel, Phys. Rev. A **42**, 2126 (1990).

[2] T. Schilling, S. Pronk, B. Mulder, and D. Frenkel, Phys. Rev. E. **71**, 036138 (2005).

[3] A. Fortini and M. Dijkstra, J. Phys. Condens. Mat. **18**, L371 (2006).

[4] A. Donev, J. Burton, F. H. Stillinger, and S. Torquato, Phys. Rev. B **73**, 054109 (2006).

[5] K. Zhao, R. Bruinsma, and T. Mason, PNAS **108**, 2684 (2011).

[6] G. Bautista-Carbajal and G. Odriozola, J. Chem. Phys. **140**, 204502 (2014).

[7] C. X. Du, G. van Anders, R. S. Newman, and S. C. Glotzer, PNAS **114**, E3892 (2017).

[8] A. Santos, S. B. Yuste, and M. López de Haro, J. Chem. Phys. **153**, 120901 (2020).

[9] M. Dijkstra, R. van Roij, and R. Evans, Phys. Rev. E **63**, 051703 (2001).

[10] E. C. Oguz, M. Marechal, F. Ramiro-Manzano, I. Rodriguez, R. Messina, F. Meseguer, and H. Löwen, Phys. Rev. Lett. **109**, 218301 (2012).

[11] C. Avendano and F. A. Escobedo, Soft Matter **8**, 4675 (2012).

[12] D. de las Heras, Y. Martínez-Ratón, L. Mederos, and E. Velasco, J. Mol. Liq. **185**, 13 (2013).

[13] G. Cinacchi and A. Tani, **141**, 154901 (2014).

[14] H. B. Kolli, G. Cinacchi, A. Ferrarini, and A. Giacometti, Faraday Discuss. **186**, 171 (2016).

[15] M. Khadilkar and F. Escobedo, Soft Matter **12**, 1506 (2016).

[16] P. Gurin, S. Varga, and G. Odriozola, Phys. Rev. E **94**, 050603 (2016).

[17] P. Gurin, G. Odriozola, and S. Varga, Phys. Rev. E **95**, 042610 (2017).

[18] E. G. Teich, G. van Anders, D. Klotsa, J. Dshemuchadse, and S. C. Glotzer, PNAS **113**, E669 (2016).

[19] S. Hashemi, Braz. J. Phys. **49**, 321 (2019).

[20] W. Jin, H. K. Chan, and Z. Zhong, Phys. Rev. Lett. **124**, 248002 (2020).

[21] M. Neudecker, S. Ulrich, S. Herminghaus, and M. Schroter, Phys. Rev. Lett. **111**, 028001 (2013).

[22] M. González-Pinto, F. Borondo, Y. Martínez-Ratón, and E. Velasco, Soft Matter **13**, 2571 (2017).

[23] M. González-Pinto, J. Renner, D. de las Heras, Y. Martínez-Ratón, and E. Velasco, New J. Phys. **21**, 033002 (2019).

[24] K. Asencio, M. Acevedo, I. Zuriguel, and D. Maza, Phys. Rev. Lett. **119**, 228002 (2017).

[25] E. Basurto, C. Haro-Pérez, C. Vargas, and G. Odriozola, Phys. Chem. Chem. Phys. **20**, 27490 (2018).

[26] P. M. Chaikin and T. C. Lubensky, *Principles of Condensed Matter Physics* (Cambridge University Press, Cambridge, England, 2000).

[27] J. P. Hansen and I. R. McDonald, *Theory of Simple Liquids*, 4th ed. (Academic Press, Amsterdam, 2013).

[28] R. Zallen, *The Physics of Amorphous Solids* (John Wiley and Sons, New York, 1983).

[29] K. He, D. Mo, T. Ye, and W. Huang, Comput. Ind. Eng. **66**, 1049 (2013).

[30] M. Mosayebi, D. K. Shoemark, J. M. Fletcher, R. B. Sessions, N. Linden, D. N. Woolfson, and T. B. Liverpool, PNAS **114**, 9014 (2017).

[31] R. J. Hunter, *Foundations of Colloid Science*, 2nd ed. (Oxford University Press, New York, 2001).

[32] R. K. Cersonsky, G. van Anders, P. M. Dodd, and S. C. Glotzer, PNAS **115**, 1439 (2018).

[33] S. Torquato, *Random Heterogeneous Materials: Microstructure and Macroscopic Properties* (Springer, 2002).

[34] A. Donev, S. Torquato, and F. H. Stillinger, J. Comput. Phys. **202**, 765 (2005).

[35] M. Moradi and F. Taghizadeh, Int. J. Mod. Phys. C **20**, 337 (2009).

[36] M. Moradi, S. Hashemi, and F. Taghizadeh, Phys. A **389**, 4510 (2010).

[37] A. Pankratov, T. Romanova, and I. Litvinchev, Wireless Netw. (2018), 10.1007/s11276-018-1890-1.

[38] T. Ras, R. Schilling, and M. Weigel, Phys. Rev. Lett. **107**, 215503 (2011).

[39] A. Donev, F. H. Stillinger, P. M. Chaikin, and S. Torquato, Phys. Rev. Lett. **92**, 255506 (2004).

[40] P. Pfleiderer and T. Schilling, Phys. Rev. E **75**, 020402 (2007).

[41] M. Radu, P. Pfleiderer, and T. Schilling, J. Comp. Phys. **131**, 164513 (2009).

[42] G. Bautista-Carbajal, A. Moncho-Jordá, and G. Odriozola, J. Chem. Phys. **138**, 064501 (2013).

[43] A. P. Lyubartsev, A. A. Martinovski, S. V. Shevkunov, and P. N. Vorontsov-Velyaminov, J. Chem. Phys. **96**, 1776 (1992).

[44] K. Hukushima and K. Nemoto, J. Phys. Soc. Jpn. **65**, 1604 (1996).

[45] S. Varga, Y. Martínez-Ratón, E. Velasco, G. Bautista-Carbajal, and G. Odriozola, Phys. Chem. Chem. Phys. **18**, 4547 (2016).

[46] G. Bautista-Carbajal, P. Gurin, S. Varga, and G. Odriozola, Sci. Rep. **8**, 8886 (2018).

[47] E. Basurto, P. Gurin, S. Varga, and G. Odriozola, Phys. Rev. Res. **2**, 013356 (2020).

[48] T. Okabe, M. Kawata, Y. Okamoto, and M. Mikami, Chem. Phys. Lett. **335**, 435 (2001).

[49] F. de J. Guevara-Rodríguez and G. Odriozola, J. Chem. Phys. **135**, 084508 (2011).

[50] G. Rickayzen, Mol. Phys. **95**, 393 (1998).

[51] J. W. Perram, M. S. Wertheim, J. L. Lebowitz, and G. O. Williams, Chem. Phys. Lett. **105**, 277 (1984).

[52] J. W. Perram and M. S. Wertheim, J. Comput. Phys. **58**, 409 (1985).

[53] A. Donev, S. Torquato, and F. H. Stillinger, J. Comput. Phys. **202**, 737 (2005).

[54] N. Rathore, M. Chopra, and J. J. de Pablo, J. Comp. Phys. **122**, 024111 (2005).

[55] L. van Hove, Physica **16**, 137 (1950).

[56] J. Cuesta and A. Sanchez, J. Stat. Phys. **115**, 869 (2004), FisEs 2002 Meeting, Tarragona, SPAIN, 2002.